

This is the peer reviewed version of the following article:

Uebe R, Keren-Khadmy N, Zeytuni N, Katzmann E, Navon Y, Davidov G, Bitton R, Pitzko JM, Schüler D, Zarivach R. 2018. The dual role of MamB in magnetosome membrane assembly and magnetite biomineralization. *Mol Microbiol* **107**:542-557.

which has been published in final form at <https://doi.org/10.1111/mmi.13899>. This article may be used for non-commercial purposes in accordance with Wiley Terms and Conditions for Use of Self-Archived Versions.

The dual role of MamB in magnetosome membrane assembly and magnetite biomineralization

René Uebe^{1#*}, Noa Keren-Khadmy^{2,3,4#}, Natalie Zeytuni^{2,3,4}, Emanuel Katzmann⁵, Yotam Navon^{3,6}, Geula Davidov^{2,3,4}, Ronit Bitton^{3,6}, Jürgen M. Pitzko⁵, Dirk Schüler¹ and Raz Zarivach^{2,3,4*}

¹ Department of Microbiology, University of Bayreuth, Universitätsstraße 30, 95447 Bayreuth, Germany

² Department of Life Sciences, Ben-Gurion University of the Negev, P.O.B. 653, Beer-Sheva 84105, Israel

³ The National Institute for Biotechnology in the Negev, Ben-Gurion University of the Negev,
P.O.B. 653, Beer-Sheva 84105, Israel

⁴ Ilse Katz Institute for Nanoscale Science & Technology, Ben-Gurion University of the Negev, P.O.B. 653,
Beer-Sheva 84105, Israel

⁵ Max Planck Institute of Biochemistry, Department of Molecular Structural Biology, Am Klopferspitz 18,
D-82152 Martinsried, Germany

⁶ Department of Chemical Engineering, Ben-Gurion University of the Negev, P.O.B. 653, Beer-Sheva
84105, Israel

These authors contributed equally to this work

*Corresponding Authors

Keywords: Bacterial organelle, biomineralization, cation diffusion facilitators, iron transport, magnetosome biogenesis, magnetotactic bacteria, membrane invagination, structure-function analysis.

Summary

Magnetospirillum gryphiswaldense MSR-1 synthesizes membrane-enclosed magnetite (Fe_3O_4) nanoparticles, magnetosomes, for magnetotaxis. Formation of these organelles involves a complex process comprising key steps which are governed by specific magnetosome-associated proteins. MamB, a cation diffusion facilitator (CDF) family member has been implicated in magnetosome-directed iron transport. However, deletion mutagenesis studies revealed that MamB is essential for the formation of magnetosome membrane vesicles, but its precise role remains elusive. In this study, we employed a multi-disciplinary approach to define the role of MamB during magnetosome formation. Using site-directed mutagenesis complemented by structural analyses, fluorescence microscopy and cryo-electron tomography, we show that MamB is most likely an active magnetosome-directed transporter serving two distinct, yet essential functions. First, MamB initiates magnetosome vesicle formation in a transport-independent process, probably by serving as a landmark protein. Second, MamB transport activity is required for magnetite nucleation. Furthermore, by determining the crystal structure of the MamB cytosolic C-terminal domain, we also provide mechanistic insight into transport regulation. Additionally, we present evidence that magnetosome vesicle growth and chain formation are independent of magnetite nucleation and magnetic interactions, respectively. Together, our data provide novel insight into the role of the key bifunctional magnetosome protein MamB, and the early steps of magnetosome formation.

Abbreviated Summary

Magnetotactic bacteria can navigate along geomagnetic field lines due to the formation of magnetic iron minerals within unique prokaryotic organelles called magnetosomes. Here, using a multidisciplinary approach, we show that magnetosome biogenesis relies on the bi-functionality of the essential magnetosome membrane protein MamB. Our results also demonstrate that the intracellular assembly of 1D magnetosome arrays mainly depends on biotic factors.

Introduction

For navigation along geomagnetic field lines, *Magnetospirillum gryphiswaldense* MSR-1 (MSR-1) and related magnetotactic bacteria (MTB) biomineralize magnetite (Fe_3O_4) nanoparticles that reside within intracellular membranous organelles called magnetosomes (Raschdorf *et al.*, 2016). Magnetosome biogenesis requires at least four tightly interconnected key steps that are controlled by a set of ~30 different magnetosome-associated proteins (Ullrich *et al.*, 2005; Fukuda *et al.*, 2006; Uebe and Schüler, 2016). Concomitant with or following magnetosome vesicle formation through invagination of the cytoplasmic membrane, magnetosome proteins are targeted to the magnetosome membrane. Subsequent import of iron in supersaturating concentrations then allows the precisely controlled biomineralization of magnetite within magnetosomes. Depending on the growth conditions, only five to six genes are essential for iron biomineralization in MSR-1 (Lohße *et al.*, 2014; Raschdorf *et al.*, 2016). Among these are the highly conserved *mamB* and *mamM* which encode cation diffusion facilitator (CDF) homologs (Jogler *et al.*, 2009; Lefèvre and Bazylinski, 2013). CDF family proteins are found in organisms of all domains of life and were shown to exclusively export divalent metal cations from the cytoplasm into the extracellular space or intracellular compartments. As such, CDF proteins contribute to metal ion resistance, signaling or metalation of metalloproteins (Nies, 2003; Jirakulaporn and Muslin, 2004; Suzuki *et al.*, 2005), with malfunction of human CDF homologues (zinc transporters ZnT1 to ZnT10) having been linked to several diseases, such as hepatomegaly, dystonia, diabetes or Alzheimer's disease (Ohana *et al.*, 2009; Barber-Zucker *et al.*, 2016; Perez *et al.*, 2017).

Like most CDF transporters, MamB and MamM share a common two-domain fold consisting of a transmembrane domain (TMD) and a cytosolic C-terminal domain (CTD)(Nudelman and Zarivach, 2014; Kolaj-Robin *et al.*, 2015). While the TMD catalyzes metal ion transport by exploiting chemiosmotic gradients (e.g. proton-motive force), the CTD has been implicated in regulating TMD activity(Zeytuni, Uebe, Maes, Davidov, Baram, Raschdorf, Nadav-Tsubery, *et al.*, 2014). Because of their magnetosome membrane (MM) localization and their affiliation with the Fe/Zn-transporting CDF subfamily, MamB and MamM are assumed to transport ferrous iron into magnetosome vesicles(Uebe *et al.*, 2011). However, cryo-electron tomographic studies showed that MamB and MamM are also required for magnetosome vesicle formation. In a MSR-1 $\Delta mamM$ strain, only few WT-like magnetosome vesicles are formed that coexist with small, electron-dense magnetosome membrane-like structures (DMMs) which were assumed to represent immature or defective magnetosome membrane vesicles(Raschdorf *et al.*, 2016). Other than very few isolated DMMs, no magnetosome vesicles were observed in a MSR-1 *mamB* deletion mutant(Uebe *et al.*, 2011). Thus, the MSR-1 $\Delta mamB$ strain shows the most severe MM phenotype of all tested single magnetosome gene mutants(Raschdorf *et al.*, 2016).

Similar to most characterized CDF transporters, MamB and MamM have been shown to self-interact and form homodimers(Uebe *et al.*, 2011; Zeytuni, Uebe, Maes, Davidov, Baram, Raschdorf, Nadav-Tsubery, *et al.*, 2014; Zeytuni, Uebe, Maes, Davidov, Baram, Raschdorf, Friedler, *et al.*, 2014; Barber-Zucker *et al.*, 2016). However, MamB and MamM have also been suggested to form heterodimers since both proteins were shown to physically interact. Indeed, heterodimer formation among CDF proteins has been increasingly recognized(Fukunaka *et al.*,

2009; Golan *et al.*, 2015). The best characterized example involves orthologues of the mammalian ZnT5/ZnT6 zinc transporter (Fukunaka *et al.*, 2009). Within this heterodimer, only ZnT5 contributes to zinc transport (Ohana *et al.*, 2009). ZnT6, which lacks two of four residues that are required for tetrahedral zinc coordination (Asp45, Asp49, His153, and Asp157) during transport, is catalytically inactive but modulates ZnT5 zinc transport activity (Fukunaka *et al.*, 2009). In MSR-1, direct interaction between MamB and MamM is required for MamB stability, as in the absence of MamM, only low amounts of MamB could be detected (Uebe *et al.*, 2011). The structural basis for MamB instability is still unknown, even though the protein shares considerable similarity with MamM, in which the mechanisms of the TMD and the CTD are clearly defined. Additionally, homology models of MamB indicate that most residues critical for CDF activation and metal transport are conserved (Nudelman and Zarivach, 2014). However, in contrast to MamM, for which transport activity and regulation have been analyzed, MamB has not been studied in detail. Therefore, several questions remained unanswered: 1) Is MamB an active transporter? 2) If MamB acts as a conventional CDF transporter, does it share structural and functional similarities to MamM and other CDF's? and 3) Is the putative transport function of MamB coupled to its role in magnetosome membrane invagination?

To answer these questions, we initiated *in vitro* and *in vivo* studies of MamB. Our genetic and biophysical approaches revealed that MamB acts as an active transporter with similar structural and mechanistic features as MamM. Moreover, we show that MamB transport activity is essential for the initiation of magnetite nucleation, yet is not required for magnetosome vesicle formation. Thus, our study not only substantiates the key role of MamB in magnetosome formation but, importantly, also provides evidence for dual transport-

dependent and transport-independent roles for a transporter of the ubiquitous CDF family(Shusterman *et al.*, 2017).

Results

Disruption of a TMD metal-binding site abolishes magnetite biomineralization

To elucidate the role of MamB during magnetosome biogenesis, we introduced heterologous mutations into *mamB* at locations that have been previously shown to impair transport activity to varying degrees (Wei and Fu, 2006; Zeytuni, Uebe, Maes, Davidov, Baram, Raschdorf, Nadav-Tsubery, *et al.*, 2014; Zeytuni, Uebe, Maes, Davidov, Baram, Raschdorf, Friedler, *et al.*, 2014; Shusterman *et al.*, 2017). Initially, we sought to replace the MSR-1 wild type (WT) *mamB* allele within the *mamAB* operon with an allele encoding a MamB_{MSR-1}D50A exchange that disrupts a conserved metal-binding site within TMD helix 2, thereby preventing transport activity. For unknown reasons, we were unable to isolate clones carrying mutated *mamB* after gene transfer to the MSR-1 WT strain. However, the mutated allele could be successfully integrated into the *mamAB*-operon of the MSR-1 WT-like $\Delta A34$ strain that carries several deletions of non-essential MAI regions (Lohße *et al.*, 2011). The resulting mutant $\Delta A34::mamB_{MSR-1}D50A$ strain showed no magnetic alignment because of the absence of magnetite nanoparticles, even when grown at a low temperature (15°C, 2% O₂, 3 days), previously shown to enhance magnetite biomineralization and rescue some gene deletion effects (Katzmann E, Eibauer M, Lin W, Pan Y, Plitzko J, 2013; Raschdorf *et al.*, 2016) (Fig. 1A). The level of *mamB* expression by strain $\Delta A34::mamB_{MSR-1}D50A$ was similar to the WT (Fig. 1B), suggesting that TMD metal binding and subsequent transport are essential for magnetite biomineralization.

In vitro characterization of MamB-CTD

Previous studies showed that CDF transport activity is regulated by the soluble C-terminal domain. To better understand the regulation of MamB, we aimed to crystallize the CTD. However, since the MSR-1 MamB CTD could not be crystallized, we expressed and purified the MamB CTD from the related alphaproteobacterial MTB *Magnetospira* sp. QH-2 (QH-2) which shows high sequence similarity to the MSR-1 MamB CTD (41% identity and 71% similarity) (Fig. 2A). According to the size exclusion chromatogram of affinity-purified MamB_{QH-2}-CTD, the eluted protein volume corresponds to a globular dimer (Cherezov *et al.*, 2008; Zeytuni *et al.*, 2012) (Fig. S1A). Dynamic light scattering (DLS) and small angle X-ray scattering (SAXS) measurements revealed a monodisperse size distribution (Fig. S1B), with a number-averaged hydrodynamic radius (Rh) of 2.34 ± 0.13 nm. At concentrations of 5 and 10 mg mL⁻¹, scattering was similar, indicating that the molecular dimensions are independent of protein concentration over this concentration range (Fig. S1C). The radius of gyration (Rg) was ~ 2 nm, as obtained by the Guinier equation for dilute solutions. An additional parameter that can provide information about the conformation of the protein in solution is the Rg/Rh ratio. Typically, the Rg/Rh value is ~ 0.773 and ~ 2 for spherical particles and rod-like objects, respectively (Chu and Liu, 2000; Tande *et al.*, 2001). The Rg/Rh value obtained for the MamB_{QH-2}-CTD was ~ 0.87 , corresponding to a particle shaped as an elongated sphere. To obtain a three-dimensional model of the MamB_{QH-2}-CTD, we generated a dummy-ball model (DBM) from the SAXS data obtained with the 10 mg mL⁻¹ sample. The model displayed an elongated structure divided into two symmetrical parts that form a dimer (Fig. S1D).

Further support for stable dimer formation by MamB_{QH-2}-CTD was provided by X-ray crystallography-based structure determination. Purified MamB_{QH-2}-CTD was crystallized with or

without a 6xHis-Tag in two different conditions (Table S1). These conditions yielded two different crystal forms with $P2_12_12$ and $P2_12_12_1$ space groups and with two and four monomers per asymmetric unit, respectively (Fig. S2). Subsequently, two different but highly similar MamB_{QH-2}-CTD structures were observed in both asymmetric unit compositions (PDB code: 5HO3 and 5HO5, RMSD of 0.54Å) (Fig. S3A and Tables S1 and S2). Each MamB_{QH-2}-CTD monomer presents a metallochaperone-like fold (2 α -helices and 3 β -strands arranged as α - β - β - α - β) to create a V-shaped dimer. The MamB_{QH-2}-CTD V-shaped dimer presents a stable dimerization interface (239 Å²) located at the dimerization surface. The dimerization interface stability rests on interactions between four amino acid pairs (A253-F259, L256-V258L, V258-L256 and F259-A254) (Fig. S3B). Such metallochaperone-like dimerization can also be found in homologous CDF CTD structures, such as MamM, CzrB, YiiP and the *Shewanella oneidensis* YiiP homolog (SO_4475) (Table S3). The dimerization area is partially conserved between these homologs at the sequence and structure levels, since most of these interactions are hydrophobic (Fig. 2 and Fig. S3).

To probe similarities between MamB_{QH-2} CTD and other CDF CTD structures, we calculated the distances between two identical C α atom residue pairs from the top and bottom of the V-shaped dimer. In MamB_{QH-2} CTD, the Arg238-Arg238 pair (19.44Å) is located at the top of the V-shaped dimer, while the Ala254-Ala254 pair (14.48Å) is located at the bottom, close to the dimerization interface. Comparing these MamB_{QH-2} distances to similar pairs in other CDF CTD structures (Fig. S4) suggests that the bottom of the V-shape is highly stable due to limited distance changes. At the same time, the distance between the V-shape arms in the upper part of the CTD can strongly vary between different structures, ranging from 19 to 28Å (Fig. 2 B-C

and Fig. S4). To assess changes in the degree-of-openness of the V-shape, C α atom angle measurements between residues at the top and bottom of the V-shape were taken. The MamB_{QH-2} opening angle between A: Arg238, B: Ala254 and B: Arg238 was $\sim 36^\circ$ in the two MamB_{QH-2} CTD structures (Fig. S4A). Comparing the degree-of-openness values between the two MamB_{QH-2} structures to those in other CTD-CDF structures indicated that the two MamB_{QH-2} CTDs showed closer similarity to the closed, metal-bound structures of YiiP ($\sim 30^\circ$)(Lu and Fu, 2007) than to the open, metal-free structures of CzrB ($\sim 53^\circ$)(Cherezov *et al.*, 2008) and MamM-CTD ($\sim 43^\circ$)(Zeytuni, Uebe, Maes, Davidov, Baram, Raschdorf, Friedler, *et al.*, 2014) (Fig. 2B-C and Fig. S4).

The role of MamB CTD metal-binding site

Next, we tested whether the MamB_{QH-2} CTD is also able to bind divalent cations, like the CTD of MamM, and determined the significance of such binding for MamB function. To locate putative metal-binding sites, we soaked MamB_{QH-2} CTD crystals with zinc, due to its solution stability compared to iron, and determined the zinc-bound structure. The MamB CTD zinc-bound form (PDB code 5HO1) is similar to the apo-MamB_{QH-2} CTD, with only minor structural changes (RMSD difference of 0.49Å over 328 common backbone atoms) (Fig. 3A). In the zinc-bound form, each monomer is associated with two zinc ions (Zn1, Zn2). Zn1 is located at the center of the V-shape with tetrahedral coordination by three residues, His245 (NE2, bond length, 2.44Å), His283 (ND1, 2.69Å) and Asp247 (OD1, 1.91Å) from the same monomer and by one water molecule (2.44Å) (Fig. 3B). The Zn2 binding site is located at the top of the V-shape in a peripheral position with atypical coordination which creates limited interactions with adjacent

amino acids. Since this location is unique and does not appear in other CDF CTD structures, we considered it a non-specific binding site (Fig. S1E). In contrast, the MamB_{QH-2} CTD Zn1 binding site agrees with the location of the MamM_{MSR-1} cation binding site in a proposed model of MamM (Zeytuni *et al.*, 2014) and with a proposed binding site of a MamB_{MSR-1} CTD model (Fig. S1F). In these proteins, zinc binding occurs at a conserved location involving MamB_{QH-2} Asp247, MamB_{MSR-1} Asp247, and MamM_{MSR-1} Asp247, Arg283 and Glu245 respectively (Fig. 2A and S1F).

To assess whether Asp247 contributes to regulation and metal binding, we mutated this residue to alanine, as previously performed with MamM_{MSR-1} where a D249A exchange has been shown to alter TMD transport activity (Zeytuni, Uebe, Maes, Davidov, Baram, Raschdorf, Nadav-Tsubery, *et al.*, 2014). First, we determined the crystal structure of MamB_{QH-2} CTD D247A to ensure the absence of structural changes. The MamB_{QH-2} CTD D247A structure (PDB code 5HOK) is similar to the WT structures (PDB code 5HO3), with a 0.17Å RMSD which is related to error values between similar crystals (Fig. S1F). To test if the D247A exchange caused a change in the zinc ion affinity we analyzed the in-solution interaction of WT and D247A MamB CTD with ZnCl₂ using isothermal titration calorimetry (ITC). While the ITC curve of the WT MamB_{QH-2} CTD showed an exothermic binding reaction upon binding of two zinc ions per dimer no interaction with zinc ions was observed for the D247A CTD (Fig. S5). Next, the *in vivo* effects of D247A mutation were examined in the WT-like ΔA34 strain background previously used for MamB_{MSR-1} D50A analysis. Therefore, we first deleted *mamB* in strain ΔA34. The resulting ΔA34Δ*mamB*_{MSR-1} mutant pheno-copied the previously described Δ*mamB*_{MSR-1} mutant (Uebe *et al.*, 2011). No magnetite particles could be observed by transmission electron microscopy (TEM), while cryo-electron tomography (CET) only revealed a few, isolated DMM-like structures, with an average

size of 31.8 ± 7.5 nm ($n=15$, 7 cells) (Fig. 4D). While expression of *mamB*_{MSR-1}*wt* in strain $\Delta A34 \Delta mamB$ _{MSR-1} restored magnetite biomineralization to WT levels, expression of *mamB*_{MSR-1}*D247A* led to an approximately 30% reduction in the number of magnetite particles per cell, but magnetosome crystal size was not affected (Fig. 3 C-D). Thus, the MamB_{MSR-1}D247A exchange essentially pheno-copied the MamM_{MSR-1} D249A mutation (Zeytuni, Uebe, Maes, Davidov, Baram, Raschdorf, Nadav-Tsubery, *et al.*, 2014), implying that in MamB and MamM, TMD activity is regulated by a similar mechanism.

MamB is a bifunctional protein

Next, we asked whether MamB TMD metal binding and transport is correlated with magnetosome vesicle invagination. To test this, we first expressed the GFP-tagged magnetosome membrane protein MamD in the WT, as well as in the $\Delta A34::mamB$ _{MSR-1}*D50A* and $\Delta A34 \Delta mamB$ _{MSR-1} strains. Similar to the WT, MamD-GFP presented a continuous linear fluorescence signal at mid-cell in the $\Delta A34::mamB$ _{MSR-1}*D50A* strain (Fig. 4 and C). While these results suggested the formation of WT-like magnetosome vesicle chains in $\Delta A34::mamB$ _{MSR-1}*D50A*, the chain-like localization pattern of MamD-GFP was disrupted in the vesicle-free $\Delta A34 \Delta mamB$ _{MSR-1} mutant (Fig. 4B). Finally, CET analysis of $\Delta A34::mamB$ _{MSR-1}*D50A* strain cells revealed empty magnetosome membrane vesicles with an average diameter of 57.6 ± 14.7 nm (Fig. 5 and Fig. 6) aligned into closely-spaced chain-like structures (12.4 ± 7.3 nm edge-to-edge distance) at mid-cell regions (Fig. 5C and Fig. 7), thus showing that MamB has a dual role in magnetosome formation.

Recently, it has been proposed that magnetosome vesicle growth depends on the onset of biomineralization (Cornejo *et al.*, 2016). Therefore, vesicles of strain $\Delta A34::mamB_{MSR-1}D50A$ should be smaller than those of magnetite-forming strains. CET of the WT and the iron uptake mutant $\Delta Fe4$, which produces 50% smaller magnetite crystals compared to the WT, however, revealed almost similar vesicle sizes (57.9 ± 9.8 nm and 59.4 ± 12 nm, respectively) as strain $\Delta A34::mamB_{MSR-1}D50A$ (Fig. 6). Additionally, we also found no significant differences in inter vesicle spacing's between these strains indicating that magnetosome chain formation is independent of magnetic interactions (Fig. 7).

Possible MamB-based protein-protein interactions

The finding that MamB transport activity is not required for magnetosome membrane formation raises questions as to its underlying mechanism. Recently, it was suggested that MamB serves as a landmark protein that induces the formation of larger protein complexes. If this were the case, then the first step in complex formation is likely interaction between MamM and MamB, since MamB stability depends on the presence of MamM. Although it was suggested that both proteins form heterodimers supported by the interaction of their C-terminal domains (Uebe *et al.*, 2011), their mode of interaction has yet to be established. To test the likelihood of a heterodimeric interaction that would also further promote CDF regulation, we modeled a MamB-MamM CTD heterodimer. We based our model on the MamB_{QH-2} crystal structure (PDB code 5HO5) and a MamM CTD_{QH-2} model (72.7% similarity, 53.3% identity to MamM MSR-1 sequence, Fig. S6). Model analysis reveals high structural

similarities to the metallochaperone-like fold of MamB and MamM, with similar predicted metal-binding sites, electrostatic potential surface and hydrophobic dimerization interface. The heterodimer dimerization interface rests on the interactions of four amino acid pairs (D53-A290 and A254, I52-L256, I50-V258 and A48-F259) (Fig. S7). Thus, a CTD heterodimer seems to be the most plausible interaction of MamB and MamM.

To examine the putative MamB-MamM CTD interaction *in vitro*, we co-expressed and co-purified recombinant MamB and MamM CTDs from MSR-1 in *Escherichia coli*, with only the MamB-CTD bearing a 6xHis tag. The co-expressed MamB/MamM_{MSR-1} sample was subjected to affinity, ion exchange and size exclusion chromatography. The size exclusion chromatography elution profile reflected that of a ~23 kDa dimer. Subsequent SDS-PAGE analysis showed two distinct bands of similar intensities corresponding to the molecular masses of His-MamB_{MSR-1} and MamM_{MSR-1}, respectively (Fig. S8). Mass spectrometry subsequently confirmed the presence of the two proteins in the dimeric fraction (Table S6). As a control, purified MamM_{MSR-1} CTD without 6xHis-Tag was subjected to Ni-NTA affinity chromatography. Subsequent SDS-PAGE analysis showed that MamM_{MSR-1} CTD does not interact with Ni-affinity resin (Fig. S8).

Discussion

Because of its homology to the metal ion-transporting CDF protein family, MamB was speculated to play a role in magnetite biomineralization by acting as a magnetosome-directed iron transporter (Grünberg *et al.*, 2001). However, recent mutational analyses revealed that MamB is required for magnetosome membrane invagination (Murat *et al.*, 2010; Uebe *et al.*, 2011; Raschdorf *et al.*, 2016), although its precise role remained unknown. Here, we performed in-depth analysis of MamB to unveil its role during magnetosome formation.

Using site directed-mutagenesis of residues critical for CDF function, we were able to show that MamB is most likely an active transporter. Mutation of a conserved residue within the MamB_{MSR-1} transmembrane helix 2 (D50A) resulted in a strain unable to biomineralize magnetite. It has been shown for the *E. coli* CDF protein YiiP (FieF) that residue D49 (homologous residue to MamB D50) is essential for transport activity since it contributes to the coordination of metal ions during transport through the TMD (Wei and Fu, 2005; Lu and Fu, 2007). Likewise, amino acid substitution of equivalent residues in several bacterial and plant CDF proteins yielded inactive proteins (Blaudez *et al.*, 2003; Anton *et al.*, 2004; Dräger *et al.*, 2004; Desbrosses-Fonrouge *et al.*, 2005; Montanini *et al.*, 2007). This suggests that the D50A substitution within MamB_{MSR-1} also abolished its transport activity and, thus, magnetite biomineralization. In contrast to the strong effect of the TMD amino acid substitution, disruption of a metal-binding site within the regulatory CTD of MamB_{MSR-1} caused only a relatively weak phenotype. In a mutant strain expressing *mamB*_{MSR-1}D247A, we observed approximately 30% fewer particle numbers per cell, but magnetite particle sizes remained WT-like. Interestingly, substitution of the equivalent residue within the CTD of MamM_{MSR-1} (D249A)

yielded a very similar result, with WT-like sized magnetite crystals but significantly reduced particle numbers per cell (Zeytuni, Uebe, Maes, Davidov, Baram, Raschdorf, Nadav-Tsubery, *et al.*, 2014).

Crystal structures of the MamB_{QH-2} CTD presented a V-shaped, dimeric metallochaperone-like fold typical of CDFs, with the dimerization interface located at the bottom of the V-shape (Cherezov *et al.*, 2008; Lu *et al.*, 2009; Zeytuni, Uebe, Maes, Davidov, Baram, Raschdorf, Nadav-Tsubery, *et al.*, 2014). Since the MamB_{QH-2} CTD forms a dimer at several concentrations in its apo-state, our data further support the suggestion that CDF CTDs permanently form stable dimers (Zeytuni, Uebe, Maes, Davidov, Baram, Raschdorf, Nadav-Tsubery, *et al.*, 2014) and do not rely on metal ion-mediated dimerization, as suggested earlier (Lu *et al.*, 2009). MamB_{QH-2} CTD zinc-bound crystals revealed two ion-binding sites (Zn1 and Zn2). Only binding site Zn1, located in the center of the dimer cavity, is considered to be functional, given how its position and tetrahedral Zn²⁺-coordination geometry are conserved among several CDF proteins (Fig. 2A, 3B) (Nierhaus, 1990; Abate *et al.*, 2014). The significance of the Zn1 metal-binding site was shown by the inability of the D247A CTD mutant to bind zinc in ITC experiments and the decreased magnetite biomineralization upon expression of full length *mamBD247A* in a *mamB* mutant.

Altogether, these findings suggest that MamB and MamM share a similar regulation mechanism in which metal binding to the CTD induces conformational changes which activate metal transport through the TMD (Zeytuni *et al.*, 2014). Since most magnetosome genes are not regulated at the transcriptional level in MSR-1 (Wang *et al.*, 2016) the regulation of MamB and

MamM at the protein level allows MSR-1 to rapidly initiate magnetite formation as soon as iron concentration in the cytosol is raised.

Interestingly, MamB transport activity seems not to be required for magnetosome membrane invagination, as a strain synthesizing the inactive MamB_{MSR-1 D50A} protein was still able to form empty WT-like magnetosome membrane vesicles (Fig. 6). Recently, it was proposed that magnetosome membrane growth is a two-step process in which the second growth stage is initiated by the onset of biomineralization (Cornejo *et al.*, 2016). However, we were unable to detect significant differences in vesicle size between the WT, the non-magnetic $\Delta A34::mamB_{MSR-1D50A}$ strain and an iron uptake mutant with smaller magnetite crystals ($\Delta Fe4$) (Fig. 6). This indicates that magnetosome membrane growth is either a continuous process or triggered by an event preceding magnetite nucleation (e.g. complete protein assembly). Additionally, magnetosome vesicles of the $\Delta A34::mamB_{MSR-1D50A}$ strain are aligned mid-cell in closely spaced chains, as is vesicle spacing in magnetite-containing WT and $\Delta Fe4$ magnetosome chains (Fig. 7). Our results indicate that magnetic interactions between magnetite crystals are not required for magnetosome chain assembly. However, detection of the magnetosome membrane around large WT magnetite crystals was often obscured by electron scattering (Fig. 7C). This caused a minor bias towards vesicles from smaller magnetite crystals having slightly higher edge-to-edge spacing than large particles (Fig. 7D). Thus, in the WT, magnetic interactions between neighboring particles may lead to slightly more compact magnetosome chains but, according to our results, this effect seems to be restricted to only a few nm in the central parts of the magnetosome chain. Therefore, our results, in agreement with previous suggestions (Faivre *et al.*, 2010; Klumpp and Faivre, 2012; Cornejo *et al.*, 2016),

provide the first *in vivo* evidence for the formation of a compact magnetosome vesicle chain being mainly driven by biotic factors, such as the actin-like MamK filament which shows dynamic pole-to-center treadmilling behavior (Toro-Nahuelpan *et al.*, 2016). Magnetic interactions between mature magnetosomes in the WT may, however, also facilitate magnetosome chain formation by helping to distinguish between empty or filled magnetosomes. This could be achieved by acting as docking sites for further magnetite-containing magnetosomes (Faivre *et al.*, 2010). Finally, the observation that magnetosome membrane invagination is independent of MamB transport activity further strengthens the idea that MamB serves as a landmark protein for the assembly of an interaction network with other magnetosome membrane proteins that, in turn, may induce membrane curvature and vesicle formation (Nudelman and Zarivach, 2014; Raschdorf *et al.*, 2016).

One known interaction of MamB involves MamM, which protects MamB from degradation (Uebe *et al.*, 2011). It has been suggested that interaction between the two CDF transporters MamM and MamB partially depends on the interaction of their CTDs (Uebe *et al.*, 2011). Here, we showed that both CTDs indeed interact, as we were able to co-purify the Mam_{MSR-1} CTD with the MamB_{MSR-1} CTD while maintaining the metal-binding site position in our modelled heterodimer, as compared to the homodimeric crystal structures. However, we cannot exclude the possibility that this is the only mode of interaction. For example, we noticed an alternative mode of interaction within one of our crystal structures in which the MamB-CTD interacted with the MamM-CTD in a β -strand pairing manner (Fig. S7). Since the β -sheet backbone of MamB_{QH-2}, β -strand 1, is exposed to the protein surface (PDB codes 5HO3 and 5HO5), it could interconnect the CTDs of the two magnetosome CDF proteins MamB and

MamM by a beta-sheet bridge. The feasibility of such interaction is also supported by the MamM_{MSR-1} structure, where the flexible C-terminal region adopts similar β -strand pairing (PDB code 3W8P). Still, further studies are needed to determine which mode of interaction occurs, this time considering the possible interactions that take place at the trans-membrane region of the MamB-MamM complex.

Overall, our study not only revealed novel insights into the role of the essential CDF transporter MamB during magnetosome formation but also into the mechanism of magnetosome vesicle and chain formation. Furthermore, we have provided evidence for a bifunctional CDF protein involved in two distinct processes (Shusterman *et al.*, 2017), namely involvement in transport-independent (magnetosome vesicle formation) and transport-dependent (magnetite nucleation) events. Together, our findings shed new light on a possible complex network of CDF proteins in mammalian systems.

Experimental Procedures

Bacterial strains, oligonucleotides and plasmids for in vivo characterization

Bacterial strains, plasmids and oligonucleotides used in this study are listed in Table S4. All strains were cultivated in Luria broth (LB, *E. coli*) or modified flask standard medium (FSM, MSR-1), as described previously (Lohße *et al.*, 2016).

mamB_{MSR-1} deletion mutagenesis and allelic exchange

For deletion mutagenesis of *mamB*, the method of Raschdorf (Raschdorf *et al.*, 2014) was used. Briefly, up- and downstream flanking regions of *mamB* were PCR-amplified using the primer pairs dmamB_do_Fw /Rev and dmamB_up_Fw /Rev, respectively. After gel purification of the resulting PCR products, both fragments were fused by overlap extension PCR using the phosphorylated primer pair dmamB_up_Fw/dmamB_do_Rev. The fused deletion construct was subsequently ligated into an EcoRV digested, dephosphorylated pORFM-Galk vector. After sequence verification, the deletion vector was transferred to MSR-1 by conjugation. Exconjugants were selected by growth on FSM-kanamycin plates for 5d at 30°C and 1.5% O₂. Several colonies were then transferred to fresh FSM medium and incubated twice for 24 h at 30°C and 1.5% O₂ before they were plated on FSM agar which was supplemented with 2.5% galactose and 100 ng ml⁻¹ anhydrotetracycline for counterselection. After 5 d incubation at 30°C and 1.5% O₂, the resulting colonies were screened for the loss of *mamB* by PCR. For allelic exchange of *mamBD50A* for *mamB*, the genomic *mamQRBS* region was PCR-amplified using the phosphorylated primers MamQ_Fw_Kpn and MamS_Rev_Sac. After ligation into the EcoRV-digested, dephosphorylated pORFM-Galk vector, inverse PCR with phosphorylated mutagenesis

primers MamBD50A_Fw and MamBD50A_Rev was performed to yield the mutagenesis vector pOR-*mamBD50A*. Exchange of *mamBD50A* for *mamB* against was performed as described above for the deletion of *mamB* and verified by sequencing.

Trans-complementation assays

For trans-complementation of $\Delta A34\Delta mamB_{MSR-1}$, the plasmids pBam1- P_{mamG} -*mamBwt* and pBam1- P_{mamG} -*mamBD247A* were transferred into $\Delta A34\Delta mamB_{MSR-1}$ by conjugation. After plasmid transfer, exconjugants were grown on FSM-kanamycin plates to select for transposition of pBAM mini-Tn5 transposons. Subsequently, the average magnetic response (C_{mag}) of three independent exconjugants was assayed. Cells were aligned at different angles relative to the light beam of a UV-vis spectrophotometer (Ultrospec 2100 pro, GE Bioscience, Marlborough, MA) using a permanent magnet. The ratio of the maximum and minimum scattering intensities (C_{mag}) was correlated with the average number of magnetic particles. The expression of *mamB*_{MSR-1} and its site-directed variants was tested by separation of whole cell protein (10 μ g) by SDS-PAGE (12%) and subsequent western blot analysis, as previously described (Uebe *et al.*, 2011).

Fluorescence microscopy

For fluorescence microscopy, the plasmid pBam-Tet-*mamD*-GFP was transferred into different MSR-1 strains by conjugation. Exconjugants were screened for successful transposition of the mini-Tn5 transposon by PCR and subjected to wide-field epi-fluorescence microscopy. Four μ l samples of MSR-1 overnight cultures were immobilized on 1% (w/v) agarose pads with FSM medium salts. The samples were imaged with an Olympus BX81 microscope equipped with a

100×UPLSAPO100XO 1.4NA objective and an Orca-ER camera (Hamamatsu) and appropriate filter sets using Olympus Xcellence software. All samples were recorded in Z-stacks with 500 ms exposure time per image. Images were processed with the ImageJ Fiji package (Schindelin *et al.*, 2012).

Transmission electron microscopy

For transmission electron microscopy (TEM), cells were adsorbed on carbon-coated copper mesh grids, air-dried (Plano, Marburg, Germany), and analyzed with a Zeiss CEM 902 A transmission electron microscope (Carl Zeiss, Oberkochen, Germany) at an accelerating voltage of 80 kV. Micrographs were taken using a 4080 × 4080 or 1350 × 1040 pixels charge-coupled device camera (Erlangshen ES500W, Gatan, Pleasanton, CA) with Gatan Digital Micrograph software (version 1.70.16) and analyzed with the ImageJ Fiji package.

Cryo-electron tomography and data analysis

Sample preparation, data acquisition, and data analysis were performed as previously described (Raschdorf *et al.*, 2013).

Expression of Magnetospira sp. QH-2 MamB in E. coli

The *mamB* CTD_{QH-2} gene was synthesized and ligated between NdeI and BamHI restriction sites of the pET28a (+) vector (Novagen). In this construct, the MamB gene was fused with DNA encoding a 6xHis tag at the N-terminus of the protein, followed by a thrombin proteolysis site (construction by Biomatik, Cambridge, ON, Canada). An *E. coli* Rosetta strain cells harboring

plasmid pET28a-MamB-CTD-QH-2 was grown in auto-induction medium(Studier, 2005) containing kanamycin (100 mg mL⁻¹) and chloramphenicol (30 mg mL⁻¹) at 37°C for 8 h. The cultivation temperature was then reduced to 27°C for a further 48 h. The cells were harvested by centrifugation at 7,438 g for 8 min at 4°C.

MSR-1 MamB and MamM CTD co-expression in E. coli

The MSR-1 *mamB* and *mamM* CTD genes were synthesized and ligated between the NdeI and BamHI restriction sites of the pET28a (+) and pET52b vectors (Novagen), respectively. The MamB gene was fused with DNA encoding a 6xHis tag at the N-terminus of the protein, followed by a thrombin proteolysis site (construction by Biomatik). An *E. coli* Rosetta strain cells harboring the plasmids pET28a-MamB-CTD-MSR-1 and pET52b-MamM-CTD-MSR-1 were grown in auto-induction medium(Studier, 2005) containing kanamycin (100 mg mL⁻¹) and chloramphenicol (30 mg mL⁻¹) and ampicillin (100mg mL⁻¹) at 37°C for 4 h. The cultivation temperature was then reduced to 27°C for a further 20 h. The cells were harvested by centrifugation at 7,438 g for 8 min at 4°C.

Site-directed mutagenesis by PCR

*mamB*_{QH-2} mutants were generated using QuickChange site-directed mutagenesis (Stratagene). Primers containing a single mutagenic site were used for PCR amplification (Table S4).

Purification of Magnetospira sp. QH-2 MamB CTD

MamB CTD-expressing cells were suspended in buffer A (50 mM Tris-HCl, pH 8, 300 mM NaCl, 20 mM imidazole, 5 mM β -mercaptoethanol, 0.01% Triton X-100) and incubated with DNase I (10 mg mL⁻¹) and protease inhibitor cocktail [100 μ M phenylmethylsulfonyl fluoride (PMSF), 1.2 μ g mL⁻¹ leupeptin and 1 μ M pepstatin A] for 20 min at 4°C. The cells were then disrupted by three cycles in a French press pressure cell at 207 MPa. Cell debris were separated by centrifugation at 43,146 g for 2 h at 4°C and the soluble fraction was applied onto a home-made gravity-flow Ni-NTA column (4 mL bed volume, 2.5 cm diameter; Bio-Rad Econo-Column chromatography column, Thermo Scientific HisPur Ni-NTA resin) pre-equilibrated with buffer A. The protein was washed with 50 mL buffer B (20 mM Tris-HCl, pH 8, 500 mM NaCl, 40 mM imidazole, 5 mM β -mercaptoethanol). The protein was washed again with buffer C (20 mM Tris-HCl, pH 8, 150 mM NaCl, 40 mM imidazole, 5 mM β -mercaptoethanol), and eluted with buffer D (20 mM Tris-HCl pH 8, 150 mM NaCl, 500 mM imidazole and 5 mM β -mercaptoethanol). The protein was concentrated to volume of 350 μ L using an Amicon Ultracel (3 kDa cutoff, Millipore) at 4°C and applied onto a size-exclusion column (HiLoad 26/60 Superdex 75, GE Healthcare Biosciences) pre-equilibrated with buffer D. Purified MamB CTD was then concentrated to 50 mg mL⁻¹ for crystallization, flash-cooled in liquid nitrogen and stored at -80°C. Throughout the purification process, protein concentrations were determined by spectrometric absorption at 280 nm using a calculated extinction coefficient of 0.493 M⁻¹ cm⁻¹.

¹. Sample purity at this stage was analyzed by SDS-PAGE.

Co-purification of MamB and MamM CTD from MSR-1 in E. coli

Sample preparation and purification were performed as previously described above for *Magnetospira* sp. QH-2 MamB CTD, except for minor modifications. Briefly, buffer B1 (20 mM Tris-HCl, pH 8, 1 M NaCl, 40 mM imidazole, 5 mM β -mercaptoethanol) was added as a preliminary wash of the Ni-NTA affinity column before buffer B. After affinity purification, the eluted proteins were loaded onto an ion-exchange column (HiTrap Q HP, 5 x 1 ml, GE Healthcare Biosciences) pre-equilibrated with buffer E (10 mM Tris-HCl, pH 8, 5 mM β -mercaptoethanol). Proteins were eluted with a salt gradient of 1 M NaCl over 60 mL (flow rate 2 mL min⁻¹). The protein was concentrated to volume of 600 μ L using an Amicon Ultracel (3 kDa cutoff, Millipore) at 4°C and applied onto a size-exclusion column (Superdex 75 Increase 10/300 GL, GE Healthcare Biosciences) pre-equilibrated with buffer D. Eluted protein fractions were concentrated to volume of 500 μ L using an Amicon Ultracel at 4°C before SDS-PAGE analysis.

MamB-MamM QH-2 heterodimer modeling

To model the MamB-MamM heterodimer, a MamM QH-2 CTD model was created using SWISS-MODEL (Guex and Peitsch, 1997), and visualized using PyMOL (DeLano, 2002). The initial homology model of MamM-CTD from *Magnetospira* sp. QH-2 was built with SWISS-MODEL, using the X-ray crystal structure of MamM MSR-1 CTD (PDB code 3W8P) as template. This model included 80 residues of the MamM QH-2 C-terminal domain.

Mass spectroscopy analysis of MamB and MamM CTD from MSR-1

Mass spectrometry was performed by the Ilse Katz Institute for Nanoscale Science and Technology, Ben-Gurion University of the Negev, using a nanoLC-2D-LTQ Orbitrap XL ETD setup.

Dynamic Light Scattering measurements

Spectra were collected using a CGS-3 apparatus (ALV, Langen, Germany). The laser power was 20 mW at the He-Ne laser line (632.8 nm). Averaged scattered intensities were measured with a ALV/LSE 5004 multiple tau digital cross correlator at 90 and 25°C. Typically, 10 runs of 30 seconds each were averaged and the correlograms were fitted using the CONTIN algorithm (Provencher, 1982). Number averaged intensities were collected and the diffusion coefficients were calculated using the Stokes-Einstein relation. The samples were filtered using a syringe filter (Millipore, 0.22 μM) 5 times and allowed to equilibrate for 10 minutes prior to measuring.

Small Angle X-ray Scattering (SAXS) measurements

SAXS experiments were also performed at the BM29-BioSAXS beamline at the European Synchrotron Radiation Facility (ESRF) in Grenoble, France. Energy of 12.5 keV corresponding to a wavelength of 0.998 Å was selected. The scattering intensity was recorded using a Pilatus 1M detector, in the interval $0.004 < q < 0.5 \text{ \AA}^{-1}$, where q is defined as $q = 4\pi/\lambda * \sin\theta$, 2θ is the scattering angle and λ is the radiation wavelength. Ten frames with 2 second exposure times were recorded for each sample. Measurements were performed in the flow mode, where samples were pumped through the capillary at a constant flow rate. The dedicated beamline softwares BsxCuBe and EDNA were used for data collection and initial processing. Further analyses and final plot preparations were performed using IGOR Pro (Ilavsky and Jemian, 2009) (WaveMetrics, Portland, OR) and the ATSAS suite (Petoukhov *et al.*, 2012).

SAXS data analysis and envelope model

The radius of gyration (R_g) was evaluated using the Guinier approximation (Guinier and Fournet, 1955). The generated envelope models (DBMs) were fitted on the core X-ray-determined wild type structure using Coot software (Emsley and Cowtan, 2004) and visualized by PyMOL (DeLano, 2002).

Crystallization

MamB_{QH-2} CTD was crystallized using the sitting-drop vapour-diffusion method at 20°C. Accordingly, 0.3 µL MamB_{QH-2} CTD solution (in buffer D) and 0.3 µL reservoir solutions containing (A) 25% PEG 3,350 0.1 M HEPES, pH 7.5, 0.2 M LiSO₄, (B) 22.5% PEG 3350, 0.1 M Mg-formate, 40% butyrolactone, (C) 0.1 M HEPES, pH 7.5, 0.2 M ammonium sulfate, 25% PEG 3350 or (D) 20% PEG 3350, 0.1 M Tris pH 8, 0.2 M MgCl₂ were mixed to form the drop. To obtain the zinc-bound state, 0.7 µL soaking solution (0.1 M HEPES, pH 7.6, 0.2 M ammonium sulfate, 27% PEG 3350 and 5 mM ZnSO₄) was added into existing crystal-containing drops. The crystal was harvested after soaking for 2.5 h.

Diffraction data collection and structure determination

Crystals were harvested and flash-cooled in liquid nitrogen with 0.1 µL 50% PEG 3350 added to the drop as a cryo-protecting solution. Diffraction data were collected using an image-plate detector system (PILATUS 6M-F 424 x 435 mm²; DECTRIS, Baden, Switzerland and MARmosaic 225 mm; MAR Research, Norderstedt, Germany). Data collection was performed at -173°C. For the MamB CTD native data set, a total of 220 frames were collected with an oscillation range of

1° and an exposure time of 2 min per image. The crystal-to-detector distance was 230.85 mm. For the zinc-bound data set, a total of 1200 frames were collected with an oscillation range of 180° and an exposure time of 0.037 min per image. The crystal-to-detector distance was 427.98 mm. For the MamB D247A data set, a total of 3600 frames were collected with an oscillation range of 0.1° and an exposure time of 0.04 min per image. The crystal-to-detector distance was 216.07 mm. The data were processed using HKL-2000(Otwinowski and Minor, 1997), XDS, Aimless and iMosflm from the CCP4i program suite(Winn *et al.*, 2011). Molecular replacement was performed using Molrep against MamB structure (PDB code 5HO3). Structure refinement was accomplished using the programs REFMAC5(Vagin *et al.*, 2004), PDB_REDO server(Joosten *et al.*, 2014) and Coot(Emsley and Cowtan, 2004). All structure figures were prepared using PyMol 1.3(DeLano, 2002).

Least-squares overlaps

R.M.S. calculations were performed with SwissPDB viewer(Guex and Peitsch, 1997) using the domain alternate fit feature to align structures on the basis of the conserved domain and to define the conformational changes of the structural homologues.

Structure Coordinates

Structures (5HO1, 5HO3, 5HO5 and 5HOK) have been submitted to the Protein Data Bank.

Isothermal titration calorimetry (ITC)

Interaction of MamB_{QH-2} CTD constructs (WT and D247A) with zinc ions was performed at a constant temperature of 25°C by titrating ZnCl₂ (0.2 mM) into the protein solution (0.1 mM).

The heat change is expressed as the electrical power (J s^{-1}). K_A and the stoichiometry, n , of the complex are also obtained by ITC (Jelesarov and Bosshard, 1999). As controls, ZnCl_2 was injected into the buffer. All measurements were compared to a reference cell containing DDW.

Supporting Information: Supporting Information is available from the Wiley Online Library or from the author.

Acknowledgments:

We are grateful to Oliver Raschdorf and Mauricio Toro-Nahuelpan (University of Bayreuth, Germany) for support with analysis of the CET data. We thank ESRF (Grenoble, France) for providing synchrotron radiation facilities beamline ID23-2 and ID14-4 and assistance during data collection, Dr. Petra Pernot for assistance in using beamline BM29-bioSAXS, and DESY (Hamburg, Germany) EMBL beamline P13. We thank Dr. Anat Shahar from the Macromolecular Crystallography Research Center (Ben-Gurion University of the Negev, Israel) and Dr. Mark Karpasas from the Ilse Katz Institute for Nanoscale Science and Technology center (Ben-Gurion University of the Negev, Israel) for LTQ Orbitrap mass spectroscopy analysis. The authors of this work are supported by the Israel Ministry of Science, Technology and Space (R.Z.), the Israel Science Foundation (grant No. 167/16; R.Z.), the European Molecular Biology Organization and CMST COST Action CM1306 (R.Z.), and the European Research Council (Proposal N° 692637 Syntomagx; D.S.). The funders had no role in study design, data collection and interpretation, or the decision to submit the work for publication.

Abate, F., Malito, E., Cozzi, R., Surdo, P. Lo, Maione, D., and Bottomley, M.J. (2014) Apo, Zn²⁺-bound and Mn²⁺-bound structures reveal ligand-binding properties of SitA from the pathogen *Staphylococcus pseudintermedius*. *Biosci Rep* **34**: 743–758.

Anna Lohße,^a Isabel Kolinko,^a Oliver Raschdorf,^{a, b} R., and Uebe, ^{a*} Sarah Borg, ^a Andreas Brachmann, ^a Jürgen M. Plitzko, ^b Rolf Müller, ^c Youming Zhang, ^d D.S. (2016) Supplement Overproduction of Magnetosomes by Genomic Amplification of Biosynthesis-Related Gene Clusters in a Magnetotactic Bacterium. **82**: 3032–3041.

Anton, A., Weltrowski, A., Haney, C.J., Franke, S., Grass, G., Rensing, C., and Nies, D.H. (2004) Characteristics of zinc transport by two bacterial cation diffusion facilitators from *Ralstonia metallidurans* CH34 and *Escherichia coli*. *J Bacteriol* **186**: 7499–7507.

Barber-Zucker, S., Uebe, R., Davidov, G., Navon, Y., Sherf, D., Chill, J.H., *et al.* (2016) Disease-Homologous Mutation in the Cation Diffusion Facilitator Protein MamM Causes Single-Domain Structural Loss and Signifies Its Importance. *Sci Rep* **6**: 31933
<http://www.nature.com/articles/srep31933>.

Blaudez, D., Kohler, A., Martin, F., Sanders, D., and Chalot, M. (2003) Poplar Metal Tolerance Protein 1 Confers Zinc Tolerance and Is an Oligomeric Vacuolar Zinc Transporter with an Essential Leucine Zipper Motif. *Plant Cell Online* **15**: 2911–2928
<http://www.plantcell.org/content/15/12/2911>
<http://www.ncbi.nlm.nih.gov/pubmed/14630973>
<http://www.plantcell.org.bases-doc.univ-lorraine.fr/content/15/12/2911.abstract>
<http://www.plantcell.org/content/15/12/2911.full.pdf>.

Cherezov, V., Höfer, N., Szebenyi, D.M.E., Kolaj, O., Wall, J.G., Gillilan, R., *et al.* (2008) Insights into the Mode of Action of a Putative Zinc Transporter CzrB in *Thermus thermophilus*. *Structure* **16**: 1378–1388.

Chu, B., and Liu, T. (2000) Characterization of nanoparticles by scattering techniques. *J Nanoparticle Res* **2**: 29–41 <http://www.springerlink.com/index/G240U7751K2646PJ.pdf>.

Cornejo, E., Subramanian, P., Li, Z., Jensen, G.J., and Komeili, A. (2016) Dynamic remodeling of the magnetosome membrane is triggered by the initiation of biomineralization. *MBio* **7**: 1–9.

DeLano, W.L. (2002) The PyMOL Molecular Graphics System, Version 0.99 Schrödinger, LLC. *Schrödinger LLC Version 1.*: <http://www.pymol.org> <http://www.pymol.org>.

Desbrosses-Fonrouge, A.G., Voigt, K., Schröder, A., Arrivault, S., Thomine, S., and Krämer, U. (2005) *Arabidopsis thaliana* MTP1 is a Zn transporter in the vacuolar membrane which mediates Zn detoxification and drives leaf Zn accumulation. *FEBS Lett* **579**: 4165–4174.

Dräger, D.B., Desbrosses-Fonrouge, A.G., Krach, C., Chardonnens, A.N., Meyer, R.C., Saumitou-Laprade, P., and Krämer, U. (2004) Two genes encoding *Arabidopsis halleri* MTP1 metal transport proteins co-segregate with zinc tolerance and account for high MTP1 transcript levels. *Plant J* **39**: 425–439.

Emsley, P., and Cowtan, K. (2004) Coot: Model-building tools for molecular graphics. *Acta Crystallogr Sect D Biol Crystallogr* **60**: 2126–2132.

Faivre, D., Fischer, A., Garcia-Rubio, I., Mastrogiacomo, G., and Gehring, A.U. (2010) Development of cellular magnetic dipoles in magnetotactic bacteria. *Biophys J* **99**: 1268–1273.

Fukuda, Y., Okamura, Y., Takeyama, H., and Matsunaga, T. (2006) Dynamic analysis of a genomic island in *Magnetospirillum* sp. strain AMB-1 reveals how magnetosome synthesis developed. *FEBS Lett* **580**: 801–812.

Fukunaka, A., Suzuki, T., Kurokawa, Y., Yamazaki, T., Fujiwara, N., Ishihara, K., *et al.* (2009) Demonstration and characterization of the heterodimerization of ZnT5 and ZnT6 in the early secretory pathway. *J Biol Chem* **284**: 30798–30806.

Golan, Y., Berman, B., and Assaraf, Y.G. (2015) Heterodimerization, altered subcellular localization, and function of multiple zinc transporters in viable cells using bimolecular fluorescence complementation. *J Biol Chem* **290**: 9050–9063.

Grünberg, K., Wawer, C., Tebo, B.M., and Schüler, D. (2001) A Large Gene Cluster Encoding Several Magnetosome Proteins Is Conserved in Different Species of Magnetotactic Bacteria. *Appl Environ Microbiol* **67**: 4573–4582.

Guex, N., and Peitsch, M.C. (1997) SWISS-MODEL and the Swiss-PdbViewer: An environment for comparative protein modeling. *Electrophoresis* **18**: 2714–2723.

Guinier, A., and Fournet, G. (1955) Small angle scattering of X-rays. *J Polym Sci* **1**: 268.

Ilavsky, J., and Jemian, P.R. (2009) Irena: Tool suite for modeling and analysis of small-angle scattering. *J Appl Crystallogr* **42**: 347–353.

Jelesarov, I., and Bosshard, H.R. (1999) Isothermal titration calorimetry and differential scanning calorimetry as complementary tools to investigate the energetics of biomolecular recognition. *J Mol Recognit* **12**: 3–18.

Jirakulaporn, T., and Muslin, A.J. (2004) Cation diffusion facilitator proteins modulate Raf-1 activity. *J Biol Chem* **279**: 27807–27815.

Jogler, C., Kube, M., Sch?bbe, S., Ullrich, S., Teeling, H., Bazylnski, D.A., *et al.* (2009) Comparative analysis of magnetosome gene clusters in magnetotactic bacteria provides further evidence for horizontal gene transfer. *Environ Microbiol* **11**: 1267–1277.

Joosten, R.P., Long, F., Murshudov, G.N., and Perrakis, A. (2014) The *PDB_REDO* server for macromolecular structure model optimization. *IUCr* **1**: 213–220
<http://dx.doi.org/10.1107/S2052252514009324>.

Katzmann E, Eibauer M, Lin W, Pan Y, Plitzko J, S.D. (2013) Analysis of magnetosome chains in magnetotactic bacteria by magnetic measurements and automated image analysis of electron micrographs. *Appl Environ Microbiol* **79**: 7755–7762.

Klumpp, S., and Faivre, D. (2012) Interplay of magnetic interactions and active movements in the formation of magnetosome chains. *PLoS One* **7**: 1–11.

Kolaj-Robin, O., Russell, D., Hayes, K.A., Pembroke, J.T., and Soulimane, T. (2015) Cation diffusion facilitator family: Structure and function. *FEBS Lett* **589**: 1283–1295
<http://dx.doi.org/10.1016/j.febslet.2015.04.007>.

Lefèvre, C.T., and Bazylnski, D. a (2013) Ecology, diversity, and evolution of magnetotactic bacteria. *Microbiol Mol Biol Rev* **77**: 497–526 <http://www.ncbi.nlm.nih.gov/pubmed/24006473>.

Lohße, A., Borg, S., Raschdorf, O., Kolinko, I., Tompa, É., Pósfai, M., *et al.* (2014) Genetic Dissection of the mamAB and mms6 Operons Reveals a Gene Set Essential f.pdf. *J Bacteriol* **196**:

2658–2669.

Lohße, A., Ullrich, S., Katzmann, E., Borg, S., Wanner, G., Richter, M., *et al.* (2011) Functional analysis of the magnetosome Island in magnetospirillum gryphiswaldense: The mamAB operon is sufficient for magnetite biomineralization. *PLoS One* **6**.

Lu, M., Chai, J., and Fu, D. (2009) Structural basis for autoregulation of the zinc transporter YiiP. *Nat Struct Mol Biol* **16**: 1063–1067.

Lu, M., and Fu, D. (2007) Structure of the zinc transporter YiiP. *Science* **317**: 1746–8.

Montanini, B., Blaudez, D., Jeandroz, S., Sanders, D., and Chalot, M. (2007) Phylogenetic and functional analysis of the Cation Diffusion Facilitator (CDF) family: improved signature and prediction of substrate specificity. *BMC Genomics* **8**: 107.

Murat, D., Quinlan, A., Vali, H., and Komeili, A. (2010) Comprehensive genetic dissection of the magnetosome gene island reveals the step-wise assembly of a prokaryotic organelle. *Proc Natl Acad Sci U S A* **107**: 5593–5598.

Nierhaus, K.H. (1990) Perspectives in Biochemistry. *Biochemistry* **29**: 4997–5008
<http://pubs.acs.org/doi/abs/10.1021/bi00473a001>.

Nies, D.H. (2003) Efflux-mediated heavy metal resistance in prokaryotes. *FEMS Microbiol Rev* **27**: 313–339.

Nudelman, H., and Zarivach, R. (2014) Structure prediction of magnetosome-associated proteins. *Front Microbiol* **5**: 1–17.

Ohana, E., Hoch, E., Keasar, C., Kambe, T., Yifrach, O., Hershinkel, M., and Sekler, I. (2009)

Identification of the Zn²⁺ binding site and mode of operation of a mammalian Zn²⁺ transporter. *J Biol Chem* **284**: 17677–17686.

Otwinowski, Z., and Minor, W. (1997) Processing of X-ray diffraction data collected in oscillation mode. *Methods Enzymol* **276**: 307–326.

Perez, Y., Shorer, Z., Liani-Leibson, K., Chabosseau, P., Kadir, R., Volodarsky, M., *et al.* (2017) SLC30A9 mutation affecting intracellular zinc homeostasis causes a novel cerebro-renal syndrome. *Brain* **140**: 928–939.

Petoukhov, M. V, Franke, D., Shkumatov, A. V, Tria, G., Kikhney, A.G., Gajda, M., *et al.* (2012) New developments in the ATSAS program package for small-angle scattering data analysis. *J Appl Crystallogr* **45**: 342–350.

Provencher, S.W. (1982) CONTIN: A general purpose constrained regularization program for inverting noisy linear algebraic and integral equations. *Comput Phys Commun* **27**: 229–242.

Raschdorf, O., Forstner, Y., Kolinko, I., Uebe, R., Plitzko, J.M., and Schüler, D. (2016) Genetic and Ultrastructural Analysis Reveals the Key Players and Initial Steps of Bacterial Magnetosome Membrane Biogenesis. *PLoS Genet* **12**: 1–23.

Raschdorf, O., Müller, F.D., Pósfai, M., Plitzko, J.M., and Schüler, D. (2013) The magnetosome proteins MamX, MamZ and MamH are involved in redox control of magnetite biomineralization in *Magnetospirillum gryphiswaldense*. *Mol Microbiol* **89**: 872–886.

Raschdorf, O., Plitzko, J.M., Schüler, D., and Müller, F.D. (2014) A tailored galK counterselection system for efficient markerless gene deletion and chromosomal tagging in *Magnetospirillum*

gryphiswaldense. *Appl Environ Microbiol* **80**: 4323–4330.

Schindelin, J., Arganda-Carreras, I., Frise, E., Kaynig, V., Longair, M., Pietzsch, T., *et al.* (2012) Fiji: An open-source platform for biological-image analysis. *Nat Methods* **9**: 676–682.

Shusterman, E., Beharier, O., Levy, S., Zarivach, R., Etzion, Y., Campbell, C.R., *et al.* (2017) Zinc transport and the inhibition of the L-type calcium channel are two separable functions of ZnT-1. *Metallomics* **9**: 228–238 <http://xlink.rsc.org/?DOI=C6MT00296J>.

Studier, F.W. (2005) Protein production by auto-induction in high density shaking cultures. *Protein Expr Purif* **41**: 207–234.

Suzuki, T., Ishihara, K., Migaki, H., Ishihara, K., Nagao, M., Yamaguchi-Iwai, Y., and Kambe, T. (2005) Two different zinc transport complexes of cation diffusion facilitator proteins localized in the secretory pathway operate to activate alkaline phosphatases in vertebrate cells. *J Biol Chem* .

Tande, B.M., Wagner, N.J., Mackay, M.E., Hawker, C.J., and Jeong, M. (2001) Viscosimetric, hydrodynamic, and conformational properties of dendrimers and dendrons. *Macromolecules* **34**: 8580–8585.

Toro-Nahuelpan, M., Müller, F.D., Klumpp, S., Plitzko, J.M., Bramkamp, M., and Schüler, D. (2016) Segregation of prokaryotic magnetosomes organelles is driven by treadmilling of a dynamic actin-like MamK filament. *BMC Biol* **14**: 88 <http://bmcbiol.biomedcentral.com/articles/10.1186/s12915-016-0290-1>.

Uebe, R., Junge, K., Henn, V., Poxleitner, G., Katzmann, E., Plitzko, J.M., *et al.* (2011) The cation

diffusion facilitator proteins MamB and MamM of *Magnetospirillum gryphiswaldense* have distinct and complex functions, and are involved in magnetite biomineralization and magnetosome membrane assembly. *Mol Microbiol* **82**: 818–835.

Uebe, R., and Schüler, D. (2016) Magnetosome biogenesis in magnetotactic bacteria. *Nat Publ Gr* **14**: 621–637 <http://dx.doi.org/10.1038/nrmicro.2016.99>.

Ullrich, S., Kube, M., Schübbe, S., Reinhardt, R., and Schüler, D. (2005) A hypervariable 130-kilobase genomic region of *Magnetospirillum gryphiswaldense* comprises a magnetosome island which undergoes frequent rearrangements during stationary growth. *J Bacteriol* **187**: 7176–7184.

Vagin, A.A., Steiner, R.A., Lebedev, A.A., Potterton, L., McNicholas, S., Long, F., and Murshudov, G.N. (2004) REFMAC5 dictionary: Organization of prior chemical knowledge and guidelines for its use. *Acta Crystallogr Sect D Biol Crystallogr* **60**: 2184–2195.

Wang, X., Wang, Q., Zhang, Y., Wang, Y., Zhou, Y., Zhang, W., *et al.* (2016) Transcriptome analysis reveals physiological characteristics required for magnetosome formation in *Magnetospirillum gryphiswaldense* MSR-1. *Environ Microbiol Rep* **8**: 371–381.

Wei, Y., and Fu, D. (2005) Selective metal binding to a membrane-embedded aspartate in the *Escherichia coli* metal transporter YiiP (FieF). *J Biol Chem* **280**: 33716–33724.

Wei, Y., and Fu, D. (2006) Binding and transport of metal ions at the dimer interface of the *Escherichia coli* metal transporter YiiP. *J Biol Chem* **281**: 23492–23502.

Winn, M.D., Ballard, C.C., Cowtan, K.D., Dodson, E.J., Emsley, P., Evans, P.R., *et al.* (2011)

Overview of the CCP4 suite and current developments. *Acta Crystallogr Sect D Biol Crystallogr* **67**: 235–242.

Zeytuni, N., Offer, T., Davidov, G., and Zarivach, R. (2012) Crystallization and preliminary crystallographic analysis of the C-terminal domain of MamM, a magnetosome-associated protein from *Magnetospirillum gryphiswaldense* MSR-1. *Acta Crystallogr Sect F Struct Biol Cryst Commun* **68**: 927–930.

Zeytuni, N., Uebe, R., Maes, M., Davidov, G., Baram, M., Raschdorf, O., Nadav-Tsubery, M., *et al.* (2014) Cation diffusion facilitators transport initiation and regulation is mediated by cation induced conformational changes of the cytoplasmic domain. *PLoS One* **9**.

Zeytuni, N., Uebe, R., Maes, M., Davidov, G., Baram, M., Raschdorf, O., Friedler, A., *et al.* (2014) Bacterial magnetosome biomineralization - A novel platform to study molecular mechanisms of human CDF-related type-II diabetes. *PLoS One* **9**.

Figures legends:

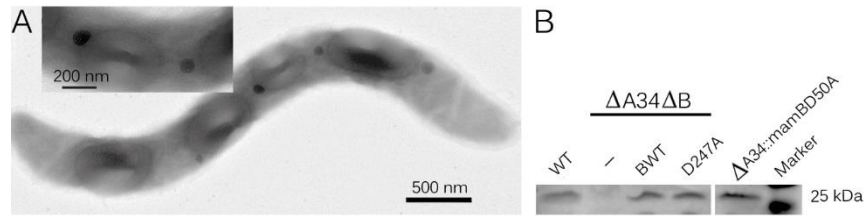
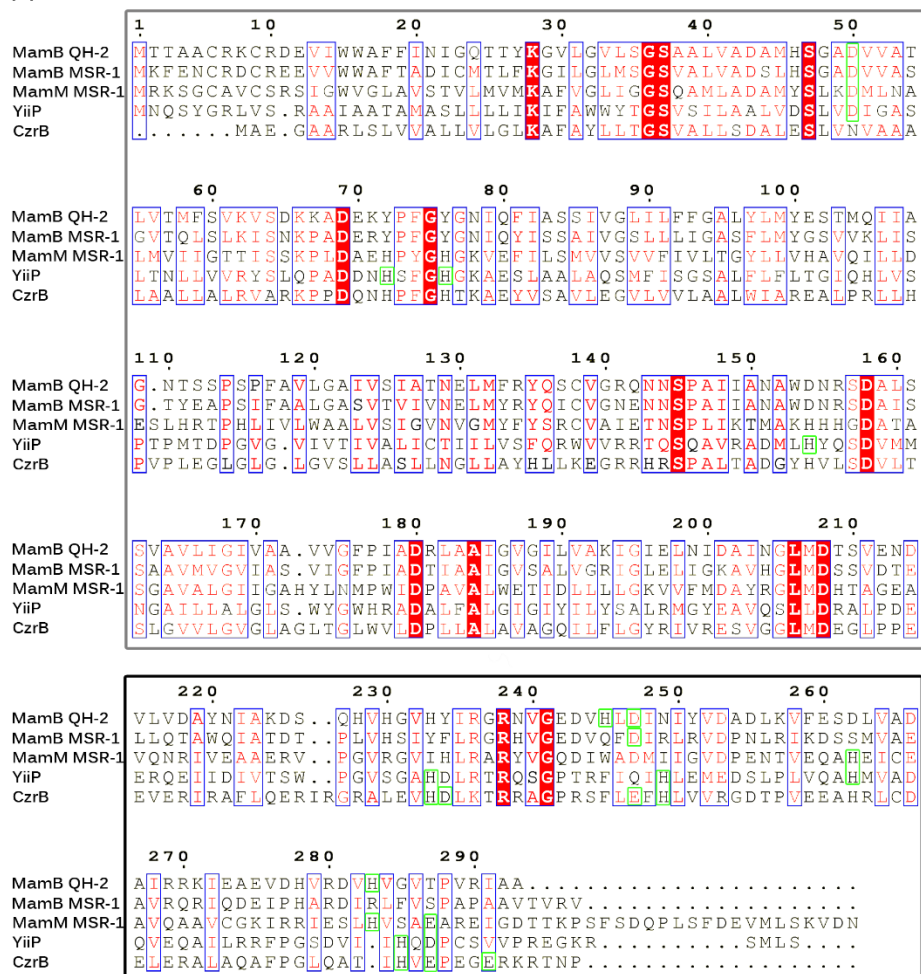
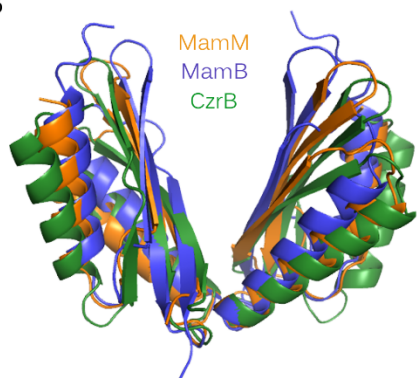


Figure 1. MamB transport activity is essential for magnetite biomineralization. (A) TEM micrograph of strain $\Delta A34::mamBD50A$. The insets show a detailed view of the cell center lacking a magnetosome chain. (B) Immunodetection of MamB in total membrane fractions of MSR-1, $\Delta A34\Delta mamB$ (-), $\Delta A34\Delta mamB::mamBwt$ (BWT), $\Delta A34\Delta mamB::mamBD247A$ (D247A) and $\Delta A34::mamBD50A$ cells.

A



B



C

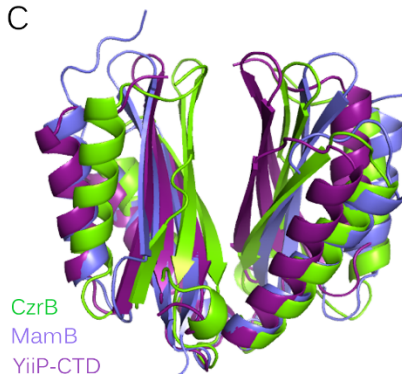


Figure 2. Comparison of CDFs. (A) Multiple sequence alignment of MamB_{QH-2} and MamB_{MSR-1} with the functionally characterized bacterial CDF proteins MamM_{MSR-1}, YiiP, and CzrB. Residues that participate in metal ion-binding are highlighted in green. The trans-membrane domain and

cytosolic C-terminal domain are framed in gray and black, respectively. The blue and red frames highlight similar and identical sequences, respectively. (B) Structural overlay of MamB_{QH-2}, MamM and CzrB CTD apo-form structures (PDB codes: 5HO5, 3W5Y and 3BYP, respectively). (C) Structural overlay of MamB_{QH-2}, CzrB and YiiP-CTD CTD metal-bound structures (PDB codes: 5HO1, 3BYR and 3H90, respectively).

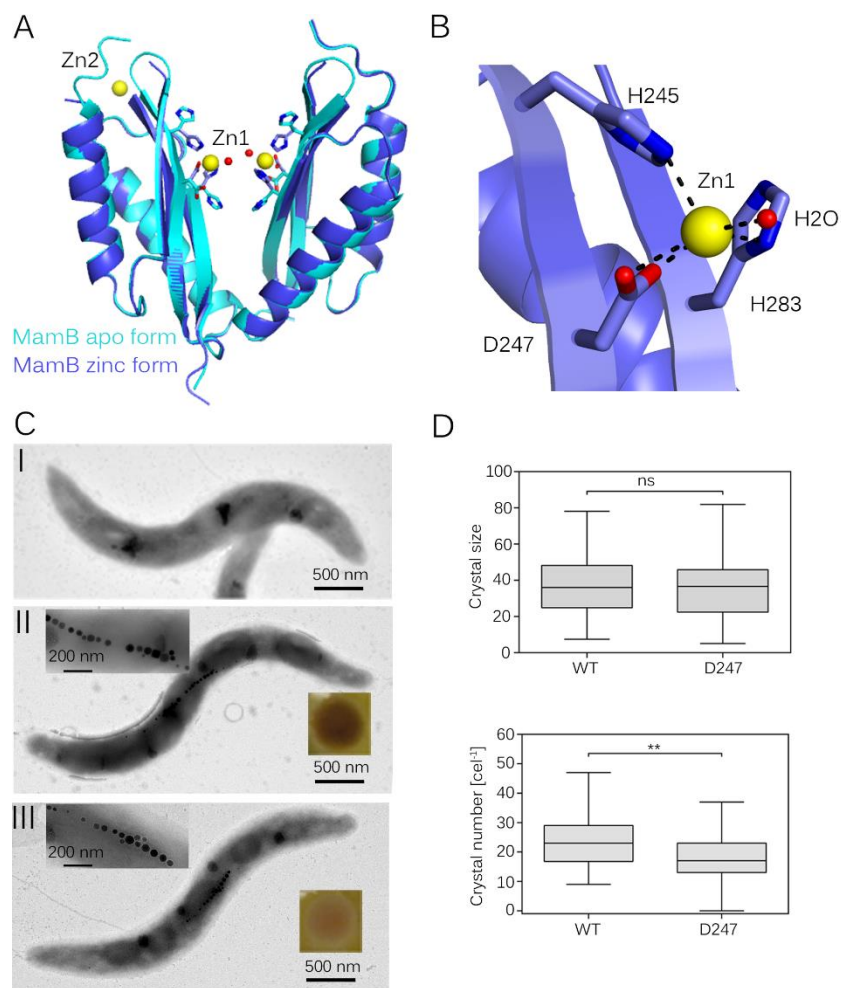


Figure 3. MamB_{QH-2} CTD cation-binding sites and *in vivo* effects of *mamB*_{MSR-1} deletion and complementation. (A) Structural overlay of MamB-CTD apo and metal-bound structures (PDB

codes 5HO1 and 5HO5). (B) Close-up view of the tetrahedral MamB-CTD zinc-binding site (Zn1) at the center of the V-shaped dimer. Zn1 is coordinated by three residues and one water molecule. Zinc ions are colored yellow, nitrogen is colored blue, and oxygen and water are in red. (C) TEM micrographs of MSR-1 *mamB* deletion strain (I) and after complementation with *mamBwt* (II) or *mamBD247A* (III). Insets show a detailed view of the magnetosome chain and color of the cell pellet, respectively. (I) Strain $\Delta A34\Delta mamB$. (II) strain $\Delta A34\Delta mamB::mamBwt$ (III) strain $\Delta A34\Delta mamB::mamBD247A$. (D) Box plots showing the number of magnetite crystals per cell and crystal size distribution (lower and upper panels, respectively) of the $\Delta A34\Delta mamB::mamBwt$ and $\Delta A34\Delta mamB::mamBD247A$ strains grown at 2% O₂ for 24 h at 28°C. The statistical significance of alterations from the strain expressing wild-type MamB was tested using a two-tailed Mann-Whitney test (**, P<0.01; ns, not significant; see Table S5 for details).

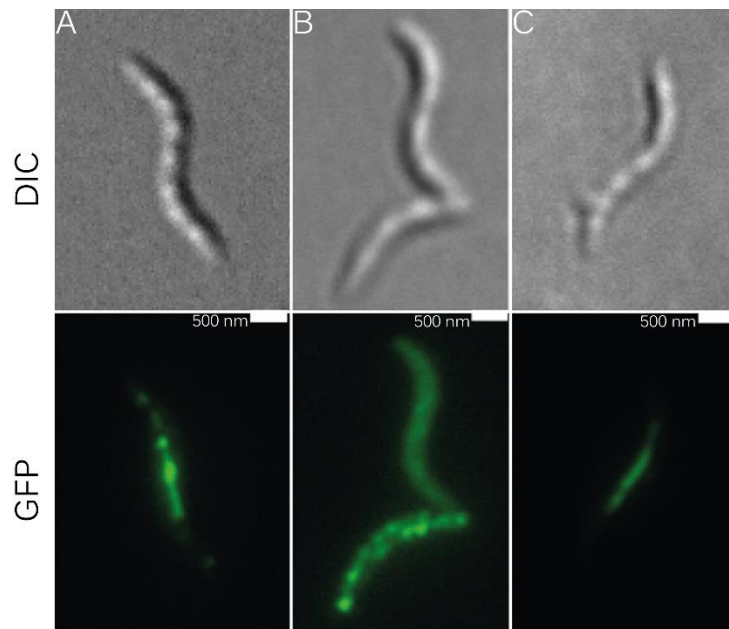


Figure 4. Localization of MamD–GFP in different MSR-1 *mamB* mutant strains. (A) MSR-1::MamD-GFP. (B) $\Delta A34\Delta mamB::MamD$ -GFP. (C) $\Delta A34::mamBD50A::MamD$ -GFP.

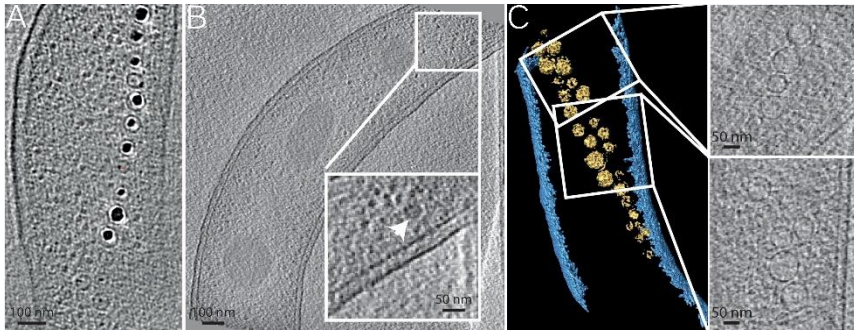


Figure 5. Cryo-electron tomograms of MSR-1 WT and different *mamB* mutant strains. (A) Section of x-y slice from tomogram of WT strain. (B) Section of x-y slice from tomogram of strain $\Delta A34\Delta mamB$, inset: Magnification of the boxed area showing a single putative DMM. (C) Segmented tomogram of strain $\Delta A34::mamBD50A$ and x-y slice details of the boxed areas. The inner and outer membrane of the cell are depicted in blue while magnetosome membranes are in yellow.

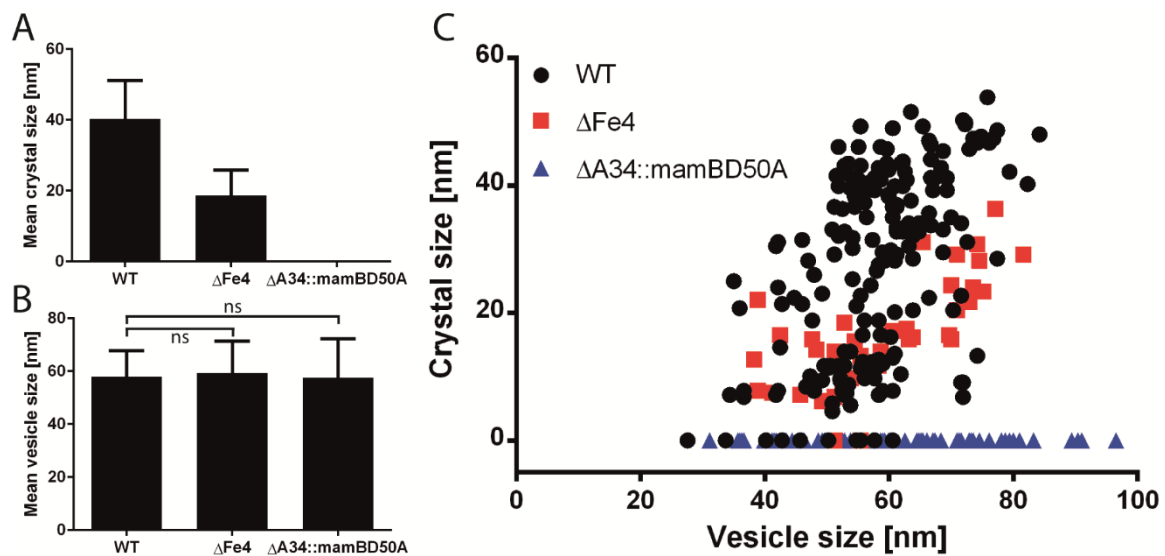


Figure 6. Magnetosome vesicle size is independent of magnetite biomineralization. A) Crystal sizes in the various strains, as analyzed by CET. Values represent the mean \pm standard deviation (nWT = 377 particles, n Δ Fe4 = 59 particles). B) Vesicle sizes in the various strains, as analyzed by CET. Values represent the mean \pm standard deviation (nWT = 188, n Δ Fe4 = 40, n Δ A34::mamBD50A = 87). ns = no significant difference, as revealed by a Mann-Whitney U-test. C) Scatter plot of vesicle size versus crystal size for magnetosomes with visible magnetosome membranes (nWT = 188, n Δ Fe4 = 40, n Δ A34::mamBD50A = 87).

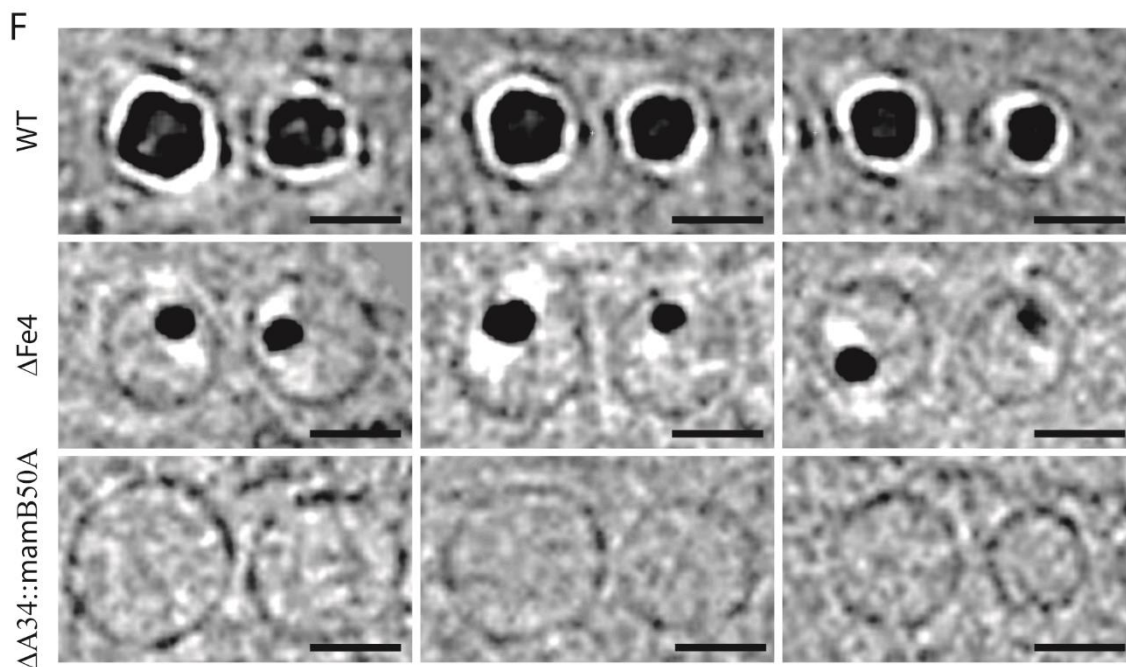
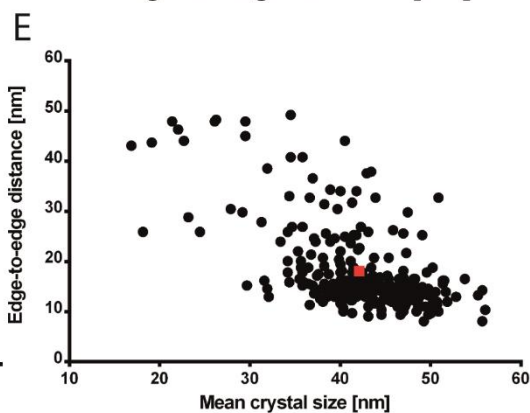
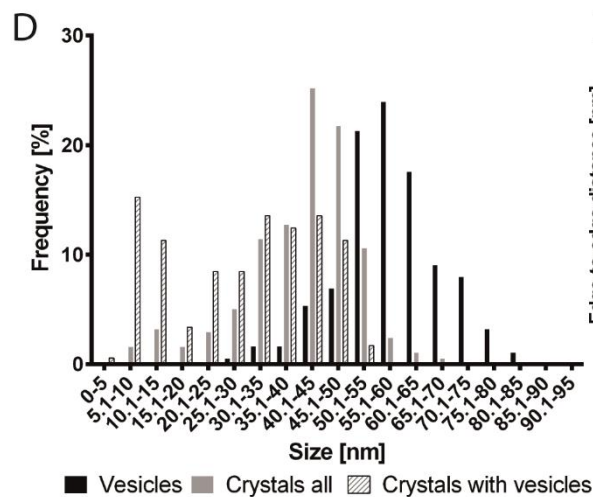
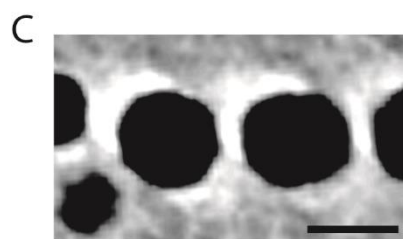
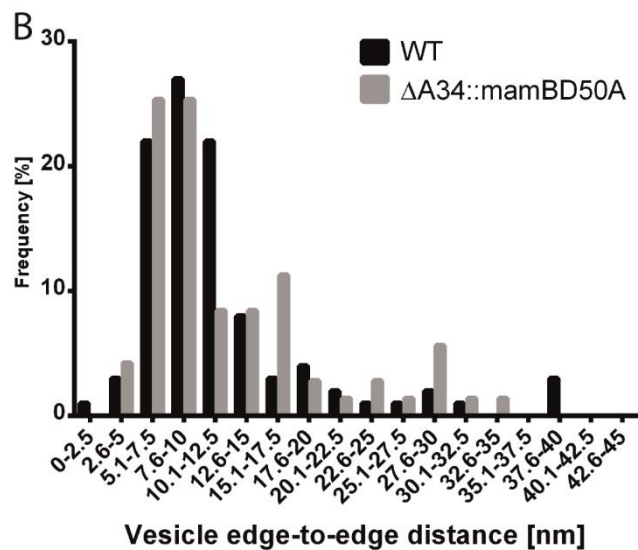
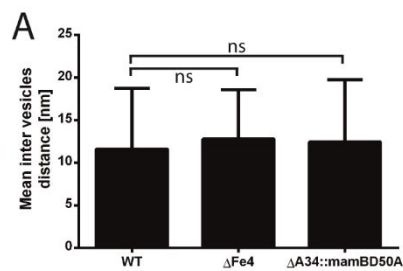


Figure 7. Magnetosome chain formation and vesicle spacing is independent of magnetic interactions. (A) Inter-vesicle distances measured from neighboring magnetosomes <50 nm from each other. Values represent the mean \pm standard deviation (nWT = 100, n Δ Fe4 = 19, n Δ A34::mamBD50A = 77). ns = no significant difference, as revealed by a Mann-Whitney U-test. (B) Vesicle edge-to-edge distance distribution between WT and the non-magnetic Δ A34::mamBD50A strain (nWT = 100, n Δ A34::mamBD50A = 77). (C) Representative x-y slice section from a WT tomogram showing larger magnetosomes. The strong artifactual white halos around the magnetite crystals (caused by the missing wedge in the tilt series) often obscure MM identification. Scale bar, 50 nm. (D) Size distribution of WT vesicles, magnetosomes crystals and magnetosome crystals with detectable magnetosome membranes in tomograms of the WT (nvesicles = 188, ncrystals = 377, ncrystals with vesicles = 177). (E) Scatter plot of mean crystal size of two neighboring magnetite crystals versus the edge-to-edge distance between the two crystals (n = 273). Distances were only measured from neighboring magnetite crystals <50 nm away. (F) Representative x-y slice sections from WT, Δ Fe4, and Δ A34::mamBD50A tomograms showing similar magnetosome spacing, independent of the presence or size of enclosed magnetite crystals. Scale bars, 50 nm.